TURBULENT SCALAR MIXING IN A SKEWED JET IN CROSSFLOW: EXPERIMENTS AND MODELING

Kevin J. Ryan
Dept. of Mechanical Engineering
Stanford University
488 Panama Mall
Stanford, CA 94305 USA
kjryan@stanford.edu

Julien Bodart
ISAE (Supaéro)
Université de Toulouse
10, avenue Edouard Belin,
BP 54032 - 31055
Toulouse CEDEX 4 France
julien.bodart@isae.fr

Mikko Folkersma
ISAE (Supaéro)
Université de Toulouse
10, avenue Edouard Belin
BP 54032 - 31055
Toulouse CEDEX 4 France
mikko.folkersma@isae.fr

Christopher J. Elkins
Dept. of Mechanical Engineering
Stanford University
488 Panama Mall
Stanford, CA 94305 USA
celkins@stanford.edu

John K. Eaton
Dept. of Mechanical Engineering
Stanford University
488 Panama Mall
Stanford, CA 94305 USA
eatonj@stanford.edu

ABSTRACT

Turbulent mixing of an inclined, skewed jet injected into a crossflow is investigated using MRI-based experiments and a high-fidelity LES of the same configuration. The MRI technique provides three-dimensional fields of mean velocity and mean jet concentration. The $30°$ skew of the jet relative to the crossflow produces a single dominant vortex which introduces spanwise asymmetries to the velocity and concentration fields. The turbulent scalar transport of the skewed jet was investigated in further detail using the LES, which was validated against the experimental measurements. Mixing was found to be highly anisotropic throughout the jet region. Isotropic turbulent diffusivity and viscosity were used to calculate an optimal value of the turbulent Schmidt number, which varies widely over the jet region and lies mostly outside of the typically accepted range $0.7 \leq Sc_t \leq 0.9$. Finally, three common scalar flux models of increasing complexity were evaluated based on their ability to capture the anisotropy of the present configuration. The higher order models were shown to better represent the turbulent scalar flux vector.

INTRODUCTION

The jet in crossflow is a canonical problem in the study of fluid mechanics due to the complicated interaction of the jet, crossflow, and incoming boundary layer. The skewed jet in crossflow has found applications as vortex generating jets used for flow control and in the turbomachinery industry for the film cooling. In this setting, the primary interest is the ability to predict the mixing of the jet fluid, or coolant, with the mainstream. The computational cost of simulating flow around a turbine blade with numerous film cooling holes limits most design stage analysis to Reynolds-Averaged Navier-Stokes (RANS) calculations. In this framework, a model for the turbulent scalar fluxes is re-

quired to close the set of equations for the transport of the passive scalar.

Among existing scalar flux models, the most common is the Gradient Diffusion Hypothesis (GDH), which represents turbulent mixing as an augmented diffusion process by way of a turbulent diffusivity, α_t. While the turbulent diffusivity can be treated as a tensor, most implementations reduce the tensor to a spatially-varying scalar. The value of α_t is typically taken as v_t/Sc_t, where the turbulent viscosity v_t is available from the RANS momentum solution and turbulent Schmidt number is commonly set in the range $0.7 \leq Sc_t \leq 0.9$. This simplified form does not allow for anisotropy, as each component of the turbulent scalar flux is proportional to the corresponding component of the scalar concentration gradient. To allow for anisotropy between components, Daly & Harlow (1970) proposed the Generalized Gradient Diffusion Hypothesis (GGDH). Abe & Suga (2001) improved on the GGDH, which they found to underpredict the streamwise component, by introducing the Higher-Order Generalized Gradient Diffusion Hypothesis (HOGGDH). This latter formulation captures the correct scaling of the streamwise and wall-normal scalar flux components for flows with scalar concentration gradients primarily in the wall-normal direction.

Rossi & Iaccarino (2009) implemented the GDH, GGDH, and HOGGDH models in a RANS calculation of a scalar released behind a square obstacle and found increased agreement between the turbulent scalar fluxes with the GGDH and HOGGDH models. While the more complicated models did show an improvement, there were still differences between model predictions and experiment. Part of the error is attributable to the use of the RANS velocity field, which has its own model uncertainty. Ling *et al.* (2015) analyzed the same three models for an unskewed jet in crossflow using a velocity fields provided by LES. They found that switching from the GDH to the GGDH or HOG-
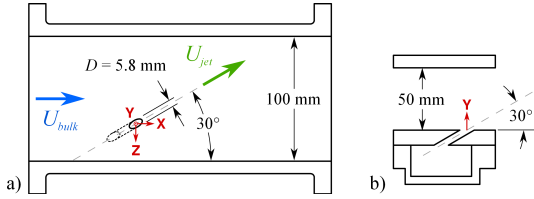
1

Figure 1. Schematic of water channel test section. a) Top view of channel showing skew angle of jet. b) Cross-section of channel viewed normal to jet hole symmetry plane. The jet feed plenum is visible below the channel. The origin of the coordinate system is the intersection of the jet hole axis with the bottom wall of the channel.

GDH improved scalar concentration predictions, but that the tuning of model parameters had a more significant effect than the switch between different models. Li *et al.* (2014) removed the specification of model parameters in the HOG-GDH by scaling an isotropic GDH-like formulation of the turbulent scalar fluxes by an anisotropic ratio determined by the anisotropy of the momentum solution. They applied this model to a $30°$ inclined hole with various skew angles and found improvements over predictions by the Realizable $k - \varepsilon$ model, but did not compare against a tuned or even standard implementation of the HOGGDH.

The present work is a combined experimental and numerical investigation of a skewed jet in crossflow. Experimental results identify important regions of the jet and validate the numerical study. Results of the numerical calculation are used to investigate the turbulent mixing in the jet and evaluate different turbulence models.

EXPERIMENTAL METHODOLOGY
Experimental Apparatus and Setup

Experiments were conducted in a closed-loop water channel with a cross-section of 100 mm x 50 mm. The jet is injected from the bottom wall of the test section through a $D = 5.8$ mm diameter hole inclined $30°$ with respect to the wall, skewed $30°$ with respect to the crossflow in the channel, and $4.1D$ in length. A schematic of the test section is shown in Figure 1. The jet is fed from below by a plenum of size 40 mm x 25.4 mm x 34.8 mm. A boundary layer trip 1 mm tall located 210 mm upstream ($X/D = -36.2$) of jet injection provides a turbulent boundary layer of height $\delta/D = 1.9$, measured at $X/D = -2$. Diffusers with grids, a honeycomb, and 2:1 area ratio contraction provide flow conditioning upstream to homogenize the inflow and reduce large scale secondary flows. Flow to the jet plenum and main channel inlet are provided by separate pumps which draw from a common reservoir. The flowrates to the jet and crossflow are continuously monitored via paddlewheel flowmeters. This jet in crossflow configuration is operated at a blowing ratio of unity, with the bulk velocities of the crossflow U_{bulk} and jet U_{jet} maintained at 0.5 m/s. The resulting jet Reynolds number is $Re_D = 2900$.

Magnetic Resonance Imaging Techniques

Three dimensional mean velocity and scalar concentration fields were acquired via magnetic resonance imaging techniques in two separate experiments. Magnetic Resonance Velocimetry (MRV) provides quantitative measurements of the flow velocity due to the sensitivity of the phase of the acquired signal to motion. Water was used as the working fluid, with copper sulfate added at a concentration of 0.06 M to enhance MRI signal magnitude. The procedure of obtaining three component velocity fields using MRV is detailed in Pelc *et al.* (1994). Thirteen individual scans, each lasting 9 minutes, were averaged to produce the final mean velocity field.

The scalar field representing the concentration of jet fluid was measured using Magnetic Resonance Concentration (MRC), where the linear relationship between copper sulfate concentration and MRI signal magnitude is employed. The jet and crossflow are fed with different concentrations of copper sulfate; for the standard configuration the jet is fed with 0.0125 M and crossflow with pure water. The inverse experiment, with copper sulfate in the crossflow and pure water in the jet, was also performed and the two resulting fields averaged to obtain the full 3D field of jet fluid concentration. Benson *et al.* (2010) document the full procedure of data acquisition for MRC measurements. Twenty scans of each standard and inverted configuration, individually lasting 4.5 minutes, are averaged to increase the signal-to-noise ratio. The molecular Schmidt number for the diffusion of copper sulfate in water is $Sc = 1500$. In the turbulent jet in crossflow, molecular diffusion is dominated by the turbulent transport and the effect of molecular diffusion on the spread of jet fluid can be considered negligible.

Both MRV and MRC experiments were performed using 3.0 Tesla GE full-body scanners at the Richard M. Lucas Center for Imaging at Stanford University. Data were acquired on a Cartesian grid measuring 0.66 mm x 0.6 mm x 0.6 mm in the streamwise, wall-normal, and spanwise directions, respectively, in a region beginning upstream of the jet and extending $20D$ downstream of injection. Measurements for MRV and MRC are acquired in Fourier space as spatial frequencies and reconstructed to 3D velocity and concentration fields. The resulting data are time-averaged over the acquisition length of the scan. Since the acquisition times for MRV and MRC are much longer than the time scales of turbulence and unsteadiness in the flow, the reconstructed fields accurately represent time-averaged quantities. Experimental uncertainty, calculated using an estimation of noise in the MRI signal and statistical variation of individual scans, is 4.3% of U_{jet} for velocity components and 5.7% for jet fluid concentration at 95% confidence.

NUMERICAL SETUP

The velocity and passive scalar concentration fields of the skewed jet in crossflow were also calculated with a high-fidelity Large Eddy Simulation (LES) using the finite-volume solver *CharLES^x*. The LES domain used the same geometry as the experiment and calculated the flow throughout the test section, including the jet hole supply plenum. The channel inlet in the simulation was located at $X/D = -40$, where a synthetic turbulent inflow is generated following the procedure used by Bodart *et al.* (2013) for a similar flow configuration. The distance between the LES inlet and jet injection was increased to allow the synthetic turbulence to reach the correct physical behavior before interacting with the jet. A uniform inlet velocity was prescribed at the experimental inlet of the jet feed plenum. The experimental boundary layer trip was not included in the simulation, so turbulence was enforced by doubling the Reynolds numbers of the jet and channel flows, thus
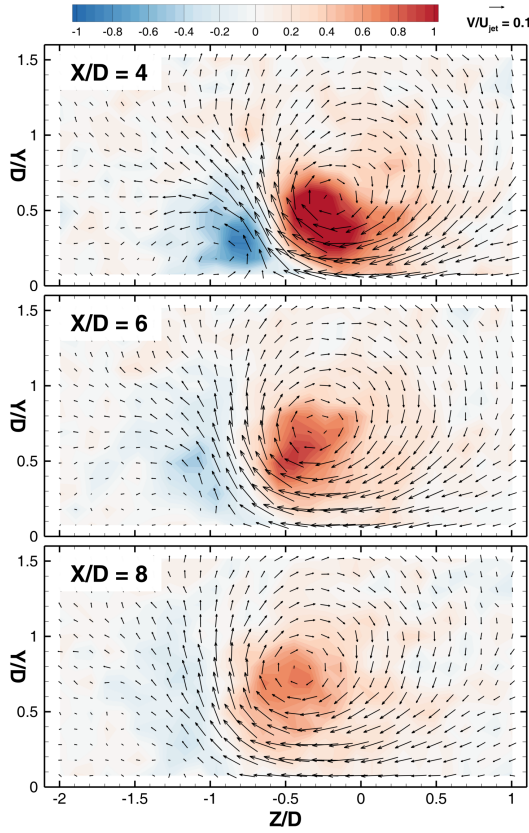
Figure 2. Color contours of normalized helicity $\vec{U} \cdot \vec{\omega} / \left(U_{jet}^2 / D \right)$ with vectors of in-plane velocity.

keeping the blowing ratio constant and recovering identical boundary layer characteristics upstream of the interaction.

The LES mesh contains a total of 101M cells, 17M of which are within the jet hole. Resolution is increased over the region of interaction of the jet and crossflow $(-1 < X/D < 10, 0 < Y/D < 2, -2 < Z/D < 1)$ to contain 18M cells with characteristic resolutions $\Delta X/D = 0.017$, $\Delta Y/D = 0.016$, and $\Delta Z/D = 0.019$. The viscous sublayer along the walls of the jet hole and bottom wall of the channel is fully resolved, with $y^+ < 1.5$. A molecular Schmidt number of $Sc = 1$ was used for transport of the passive scalar. Turbulence is expected to dominate scalar transport, so differences in molecular Sc between the experiment and LES are negligible. The subgrid-scale (SGS) momentum equation was formulated using the Vreman model, and the Reynolds analogy was used for the passive scalar with a fixed value of $Sc_{SGS} = 0.9$. Within the jet region, the SGS viscosity is mostly less than 30% of the molecular viscosity, with a local peak near 50%. The SGS model contribution can therefore be considered negligible.

LES convergence was examined by monitoring time-averaged streamwise velocity and turbulent kinetic energy along a streamwise profile within the jet at $Y/D = 0.6$, $Z/D = -0.6$. Time averages are computed from the LES during 252 time units $(T = D/U_{bulk})$, using 85,000 statistical samples. After 200 time units the monitored time averages remained unchanged within 1% and 4% for the streamwise velocity and turbulent kinetic energy, respectively, and the simulation was considered converged for first and second moment terms.
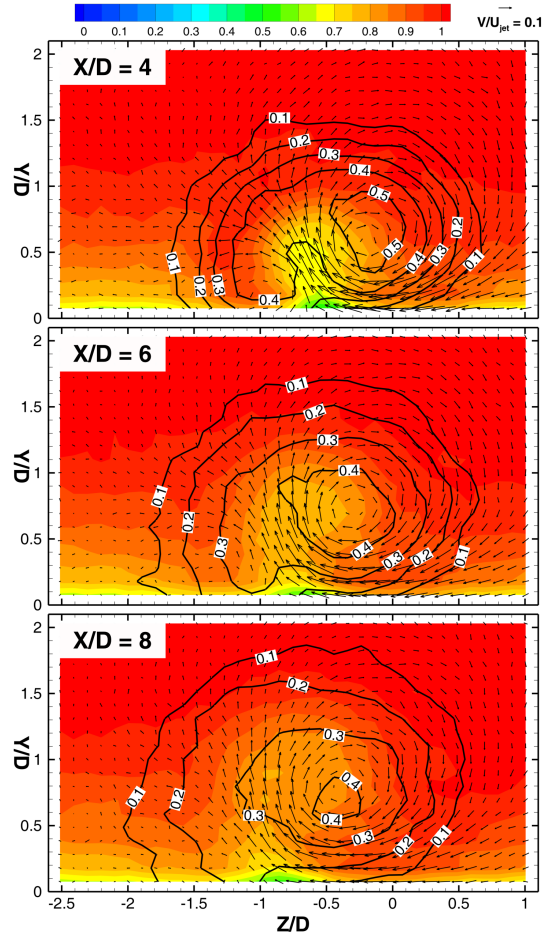

Figure 3. Color contours of normalized streamwise velocity $\overline{U}/U_{jet}$ with vectors of in-plane velocity and contours lines of jet fluid concentration.

RESULTS

Experimental results examining the features of the skewed jet in crossflow and turbulent scalar flux model evaluation are presented in the following sections. The X, Y, and Z coordinates denote streamwise, wall-normal, and spanwise coordinates (see Figure 1) and are normalized by hole diameter D. Locations within the jet will be described as if viewed from upstream; "right" is in the positive spanwise direction, "left" is negative. Velocity components are normalized by jet bulk velocity U_{jet}.

Experimental Results - Jet Features

The dominant feature of the jet in crossflow is a counter-rotating vortex pair (CVP) which develops inside the jet hole and governs much of the jet-crossflow interaction. The CVP lifts the jet off the wall and mixes crossflow fluid into the core of the jet. For the skewed jet configuration, one vortex of the pair quickly dies out after injection, leaving a single vortex to control the development of the jet. Vorticity within the jet is visualized in Figure 2 as contours of helicity, overlaid with in-plane velocity vectors. The second vortex is visible in the contour at $X/D = 4$, but this vortex quickly dissipates leaving a single vortex in the jet.

The effects of the vortex on the development of the jet are shown in Figure 3, which has color contours of stream-
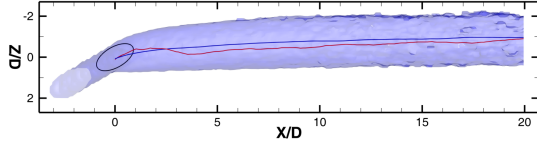
Figure 4. Top view of 10% jet fluid concentration isosurface. The red line is the locus of concentration maxima at different streamwise positions. The blue line is the area-averaged center of region enclosed by the isosurface. The black ellipse is the exit of the jet hole.

wise velocity and contour lines of jet concentration. The vortex carries low velocity fluid from the boundary layer beneath the jet up into the jet region. The vortex also entrains low concentration fluid from the crossflow into the jet region. The entrainment of slower, low concentration fluid occurs in the same location toward the left side of the jet, creating a distortion of the velocity and concentration contours. The rightmost extent of the $\overline{C} = 0.1$ contour remains at a spanwise position between $Z/D = 0.5$ and $Z/D = 0.6$ over several hole diameters of development. The left side of the jet, however, increases from a spanwise extent of $Z/D = -1.7$ to $Z/D = -2$ over the same distance. The preferential mixing at this one spanwise location has a clear effect on the lateral spread of jet fluid.

The jet concentration distribution is also linked to secondary flow features. The location of maximum jet concentration at each streamwise position correlates with the center of the jet vortex, located on the right side of the jet $-0.5 < Z/D < 0$. The asymmetry of the concentration maximum is another indication of different lateral mixing behavior. The spanwise location of the maximum concentration on each streamwise plane is plotted in Figure 4, along with the top view of the 3D isosurface of 10% jet fluid concentration and the area-weighted spanwise center of the isosurface. For $X/D > 2.5$, the location of the maximum concentration is always at a greater spanwise value than the isosurface center, confirming the observations of Figure 3. The spanwise variation in mixing behavior is important in the discussion of turbulent scalar flux models to follow.

Experimental Validation of LES

The LES was validated by comparing contours of mean jet fluid concentration and mean velocity to the experimentally-determined fields. Detailed comparisons of the mean flow features of the LES to the experiment show agreement to within experimental uncertainty. As examples, Figure 5 shows comparisons of jet fluid concentration between MRC and the LES and Figure 6 compares the streamwise velocity of the MRV and LES. The LES faithfully represents the mean velocity and concentration fields which lends confidence in the higher order moments extracted from the LES, $\overline{u_i' u_j'}$ and $\overline{u_i' c'}$.

Turbulent Scalar Flux Modeling

The experimentally-validated LES has been used to evaluate common turbulent scalar flux models. LES is an ideal tool for evaluating model performance due to the confidence in the Reynolds stress tensor components, which must otherwise be modeled if RANS were used. With correct velocity fields from the LES, model form error can be decoupled from errors of using incorrect velocity fields to
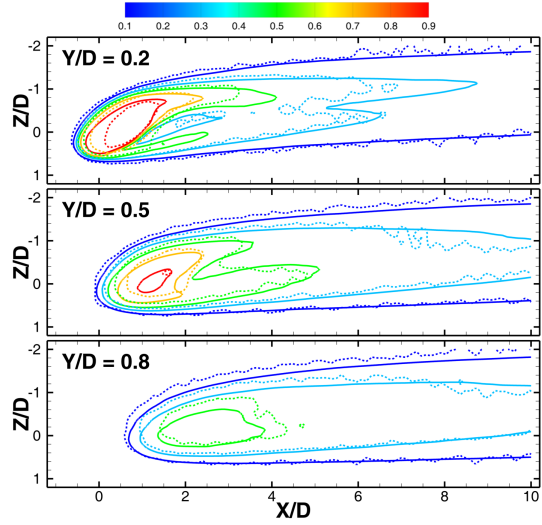

Figure 5. Comparison of MRC (- - -) and LES (——) mean concentration on wall-normal planes. Concentration contours at 0.1, 0.3, 0.5, 0.7, and 0.9 are shown.
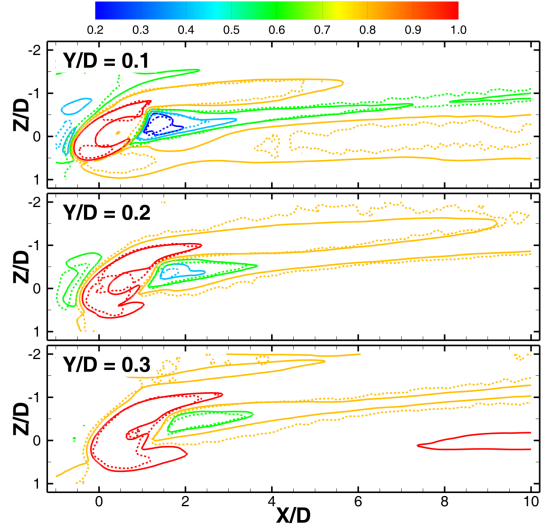

Figure 6. Comparison of MRV (- - -) and LES (——) mean streamwise velocity on wall-normal planes. Velocity contours at 0.2, 0.4, 0.6, 0.8, and 1.0 U_{jet} are shown.

calculate turbulent scalar fluxes. Therefore, the error associated directly with the turbulent scalar flux model can be isolated from its inputs, and model performance can be evaluated directly. Three models are considered and compared: the GDH, GGDH, and HOGGDH.

$$\overline{u_i' c'}_{GDH} = -\alpha_t \frac{\partial \overline{C}}{\partial x_i} \tag{1}$$

$$\overline{u_i' c'}_{GGDH} = -\alpha_C \tau_C \overline{u_i' u_j'} \frac{\partial \overline{C}}{\partial x_j} \tag{2}$$

$$\overline{u_i' c'}_{HOGGDH} = -\alpha_C \tau_C \frac{\overline{u_i' u_k'}\,\overline{u_k' u_j'}}{k} \frac{\partial \overline{C}}{\partial x_j} \tag{3}$$
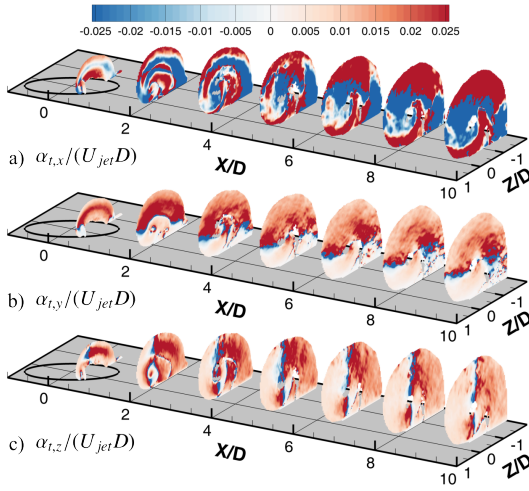
4

Figure 7. Anisotropic components of turbulent diffusivity α_t. Streamwise slices of the jet region are blanked for $\overline{C} < 0.05$ for clarity, and for $D|\nabla\overline{C}| < 0.1$ where α_t is ill-defined. Black ellipse is the exit of the jet hole.

The GDH is defined by the turbulent diffusivity α_t, which in general is spatially-varying and anisotropic, but is commonly treated as isotropic and linked to the turbulent viscosity through the Reynolds Analogy, $Sc_t = \nu_t/\alpha_t$. The turbulent Schmidt number Sc_t is typically set at a constant value in the range $0.7 \leq Sc_t \leq 0.9$. The GGDH and HOGGDH are proportional to a turbulent time scale τ_C, typically taken as $\tau_C = k/\varepsilon$, and model constant α_C.

The GGDH and HOGGDH allow for increasingly more anisotropy over the standard GDH model. To examine the anisotropy of the skewed jet in crossflow, the turbulent scalar fluxes $\overline{u_i'c'}$ and concentration gradient $\partial\overline{C}/\partial x_i$ extracted from the LES were used to calculate anisotropic components of the turbulent diffusivity, $\alpha_{t,x}$, $\alpha_{t,y}$, and $\alpha_{t,z}$. These quantities are shown in Figure 7 at several streamwise locations within the jet region. Within each component, the value of turbulent diffusivity varies significantly over the jet region. The streamwise component in Figure 7a shows large regions of counter-gradient diffusion, with negative values of $\alpha_{t,x}$. The $\alpha_{t,y}$ and $\alpha_{t,z}$ components in Figures 7bc also show evidence of counter gradient diffusion, but these are limited to small regions where the mean concentration gradient goes to zero and thus does not represent a significant contribution to the overall scalar fluxes. What is more striking about these components is the asymmetry of the diffusivity magnitude on either side of the line denoting zero concentration gradient. The top half of the jet in Figure 7b has an order of magnitude higher value of $\alpha_{t,y}$ than the bottom half of the jet, and the same trend holds for $\alpha_{t,z}$ for the left side of the jet over the right.

The ranges of $\alpha_{t,y}$ and $\alpha_{t,z}$ magnitudes are roughly the same over the jet region, while $\alpha_{t,x}$ (shown on the same scale), is up to an order of magnitude greater than the other components. This is due to the low streamwise gradients of concentration which artificially increase the value of $\alpha_{t,x}$. The magnitude of the streamwise turbulent scalar flux $\overline{u'c'}$ remains small throughout the jet region and can be considered negligible compared to the mean convective flux $\overline{U}\,\overline{C}$. The upper left region of the jet, where both $\alpha_{t,y}$ and $\alpha_{t,z}$ are positive and roughly the same magnitude, is a region where an isotropic turbulent diffusivity model would be accurate.
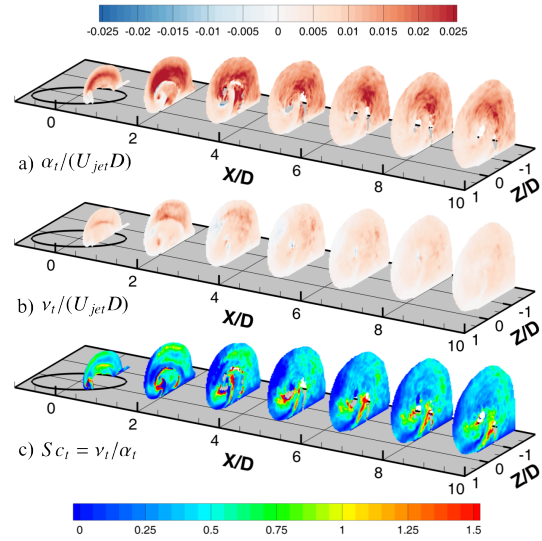

Figure 8. Isotropic a) turbulent diffusivity α_t, b) turbulent viscosity ν_t, and c) turbulent Schmidt number Sc_t. Streamwise slices of the jet region are blanked for $\overline{C} < 0.05$ for clarity, and for $D|\nabla\overline{C}| < 0.1$ where α_t and Sc_t are ill-defined. Black ellipse is the exit of the jet hole.

However, this only represents a small portion of the jet region. Interestingly, this region is the same location where the preferential mixing shown in Figure 3 occurs. Likewise, the intersection of the lines of zero concentration gradient corresponds with the location of maximum concentration of the jet and center of the jet vortex.

Although Figure 7 clearly invalidates the assumption of turbulent diffusivity isotropy, the isotropic GDH is still the most common turbulent scalar flux model employed. The LES can provide optimal isotropic, spatially-varying α_t and ν_t. These fields are used to test the assumption of a constant turbulent Schmidt number. Isotropic α_t and ν_t are found by weighting components of the turbulent scalar flux vector and Reynolds stress tensor by the mean concentration gradient $\partial\overline{C}/\partial x_i$ and mean strain rate tensor S_{ij}:

$$\alpha_t = -\overline{u_i'c'}\frac{\partial\overline{C}}{\partial x_i} \bigg/ \frac{\partial\overline{C}}{\partial x_j}\frac{\partial\overline{C}}{\partial x_j} \tag{4}$$

$$\nu_t = -\overline{u_i'u_j'}S_{ij} \bigg/ S_{kl}S_{kl} \tag{5}$$

Isotropic values of α_t and ν_t along with turbulent Schmidt number Sc_t are shown in Figure 8. Slices have been blanked where the concentration gradient magnitude $D|\nabla C| < 0.1$, where α_t and Sc_t are ill-defined. The weighting of α_t and ν_t produces fields that are almost entirely positive, prohibiting the representation of any counter-gradient diffusion. The value of Sc_t varies drastically throughout the jet as seen in Figure 8c, with most locations having $Sc_t < 0.5$ but smaller regions with $Sc_t > 1.5$. The region where $0.7 \leq Sc_t \leq 0.9$, represented in Figure 8c by green-to-yellow contours, makes up only a small part of the jet with the largest region located near jet injection in the vicinity of the shear layer mixing above and below the jet.

The abilities of the GDH, GGDH, and HOGGDH to capture the anisotropy of the skewed jet in crossflow are evaluated by comparing the predicted turbulent scalar flux
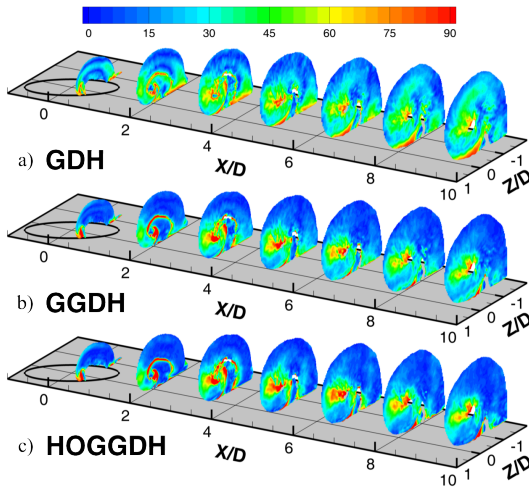
Figure 9. Angle ϕ in degrees between turbulent scalar flux vectors $\overline{u_i' c'}_{LES}$ and $\overline{u_i' c'}_{Model}$ for a) GDH, b) GGDH, and c) HOGGDH. Black ellipse is the exit of the jet hole.

vectors given by Equations 1-3 to that extracted from the LES. The more common isotropic version of the GDH is used for this analysis. To remove any bias introduced by the choice of model constants α_C, turbulent diffusivity α_t, and turbulent time scale τ_C from the analysis, the angle ϕ between the turbulent scalar flux vectors of each models and that of the LES are compared. This metric is a more direct evaluation of model ability to capture flow anisotropy.

Figure 9 shows the misalignment angles for each of the three models considered, with angle reported in degrees. Data have been blanked when $|\overline{u_i' c'}_{LES}| < 0.001$ where small deviations could produce large vector misalignment. The GDH shows significant misalignment throughout the jet region. Note that this implies that the scalar flux is not aligned with the concentration gradient. Only a small region has $\phi < 15°$, located mostly around the periphery of the jet, favoring the top and left sides. Two locations have near 90° misalignment: the first is near the bottom wall on the right side of the jet, the second is directly above this, near the location of maximum concentration identified in Figure 3.

Figure 9b shows angle misalignment for the GGDH model. The anisotropy allowable by the GGDH has significantly reduced ϕ in much of the jet region. The left and top halves of the jet now show misalignment of 15° or less, and the first two slices shown feature large regions of near-zero angle misalignment. Additionally, the near-wall region on the right side of the jet has been reduced by about 25°. The GGDH has worsened alignment in a few regions, one in particular being the middle of the right side of the jet. The region of $\phi > 60°$ has increased, and a larger area has an angle misalignment closer to 90°. The HOGGDH model makes some improvements over the GGDH, but also introduces angle misalignment in certain locations. The top and left halves of the jet are again well captured by the HOGGDH, with improvements of a few degrees over the GGDH. The most noticeable change occurs near the bottom wall on the right side of the jet. Although a thin layer of near 90° misalignment remains, the area directly above the wall has been reduced in large part below 15°. Misalignment increased in the same region as was observed with the GGDH, with a larger area near 90°. While this analysis provides an indication of a model's best ability to capture anisotropy,

the overall performance of the model when implemented will depend on the choice of model constants, not discussed here. It is expected that a spatially-varying α_C be required to match the magnitude of the turbulent scalar flux vectors.

CONCLUSIONS

Mean velocity and concentration fields of a skewed jet in crossflow were measured using MRI-based techniques. The significant feature of the skewed jet is a single vortex which governs development of the velocity and concentration fields by preferentially introducing slow, low-concentration fluid to one side of the jet. An LES of the same configuration, validated against the experiment, allowed for direct investigation of the turbulent scalar flux components in the jet region. The assumptions of isotropy and a uniform turbulent Schmidt number, commonly used in RANS calculations of this and other flows, were shown to be invalid for this jet in crossflow geometry. Three models typically used to represent the turbulent scalar fluxes, the GDH, GGDH, and HOGGDH, were evaluated based on their ability to capture scalar flux anisotropy. The GGDH and HOGGDH were found to better represent the scalar flux vector in large parts of the flow, although several areas remained unchanged or even slightly worsened with the higher order models.

REFERENCES

Abe, K. & Suga, K. 2001 Towards the development of a Reynolds-averaged algebraic turbulent scalar-flux model. *International Journal of Heat and Fluid Flow* **22** (1), 19–29.

Benson, Michael J, Elkins, Christopher J, Mobley, Paul D, Alley, Marcus T & Eaton, John K 2010 Three-dimensional concentration field measurements in a mixing layer using magnetic resonance imaging. *Experiments in Fluids* **49** (1), 43–55.

Bodart, J., Coletti, F., Bermejo-Moreno, I. & K., Eaton J. 2013 High-fidelity simulation of a turbulent inclined jet in a crossflow. Center for Turbulence Research annual research brief. Stanford University, Stanford, CA.

Daly, B. J. & Harlow, F. H. 1970 Transport equations in turbulence. *Physics of Fluids* **13** (11), 2634–2649.

Li, X., Qin, Y., Ren, J. & Jiang, H. 2014 Algebraic anisotropic turbulence modeling of compound angled film cooling validated by particle image velocimetry and pressure sensitive paint measurements. *Journal of Heat Transfer* **136** (3), 032201.

Ling, J., Ryan, K. J., Bodart, J. & Eaton, J. K. 2015 Analysis of turbulent scalar flux models for a discrete hole film cooling flow. In *Proceedings of ASME Turbo Expo*.

Pelc, N., Sommer, F., Li, K., Brosnan, T., Herfkens, R. & Enzmann, D. 1994 Quantitative magnetic resonance flow imaging. *Magnetic Resonance Quarterly* **10** (3), 125–147.

Rossi, R. & Iaccarino, G. 2009 Numerical simulation of scalar dispersion downstream of a square obstacle using gradient-transport type models. *Atmospheric Environment* **43** (16), 2518–2531.

6